Ab initio investigation of the elastic properties of bismuth-based alloys

Michael Woodcox, Joshua Young, and Manuel Smeu*
Department of Physics, Binghamton University–SUNY, Binghamton, New York 13902, USA

(Received 15 May 2019; revised manuscript received 19 August 2019; published 6 September 2019)

Density functional theory has been used to investigate the elastic properties of various Bi-based alloy materials as potential replacements of lead-based solders. We compare calculated quantities which can be used to determine the effectiveness of our proposed replacements, such as the bulk (K), shear (G), and Young's (E) moduli. We also computed the Pugh ratio ($\gamma = K/G$), a quantity that is used to estimate the ductility of a solid, for each of the alloys. The effect of spin-orbit coupling on these materials has also been investigated. By analyzing the changes in charge density as Bi is substituted, we link the predicted changes in ductility in these materials to atomistic descriptors; specifically, delocalization of the charge density is known to be a signature of increased ductility, whereas more localized charge density is typically associated with brittleness. Through Bader charge analysis we provide quantitative insight into the uniformity of charge distribution and how this alters the ductility of these alloys. By using density functional theory to calculate the elastic properties of different $Bi_{1-x}Z_x$ alloys (Z = Sb, Te, In, Sn; $0 \leqslant x \leqslant 1$), we correlate changes in ductility and corresponding changes in the electronic structure of a material. We have found that low concentrations of Sn and Te, substituted into the hexagonal crystal structure of Bi, induce significant increases in ductility.

DOI: 10.1103/PhysRevB.100.104105

I. INTRODUCTION

Bismuth is a desirable replacement for lead in many applications because they have similar properties, but Bi has a very low level of toxicity while maintaining a tunable melting point when used in alloys [1]. Although there are many different alternatives that are in use, cost, melting point, and growing health concerns related to using these replacement materials have increased the difficulty in providing industry-wide alternatives [2,3]. Along with good thermal conductivity, one of the important qualities in a good solder material is ductility. Brittle materials are not capable of accommodating the stress that occurs during deformation; thus, they will begin to crack or fracture entirely. Experimentally, Bi is found to be brittle [4–6], but it has been demonstrated that through alloying, it can be made ductile [7]. For example, it has been shown that by alloying Bi with Sb, the bulk, shear, and Young's moduli could be manipulated to create a more ductile material [7]. Previous work has also shown that by alloying Bi with other known Pb-free solders (particularly, Sn-3.5Ag-Bi), the mechanical fatigue of the solder was reduced [8,9]. For these reasons, it is believed that Bi alloys should be investigated as possible replacements for Pb-based solder [10].

The formation and synthesis of $Bi_{1-x}Sb_x$ alloys were previously studied through experiment and computation [11–13]. While much work has been done on unique phases of $Bi_{1-x}Sb_x$ alloys, it is known that these alloys form a homogeneous solid solution maintaining the $R\bar{3}m$ space group [13]. Previous studies have also provided computational and experimental insight into known, stable $Bi_{1-x}Sb_x$ compositions [7,14–17]. In those works, potential $Bi_{1-x}Sb_x$ compositions were investigated, verifying their stability and thermoelectric, transport, and elastic properties. The unique nature of the Bi-Sb alloys has shown that they exhibit thermoelectric and semiconducting behavior at particular concentrations. Thermoelectric and thermomechanical properties (such as lattice thermal conductivity) of Bi_2Te_3 have been studied extensively through computation, along with their phonon dispersion [18–20]. In that work there was an emphasis placed on the temperature dependence of the elastic properties of Bi_2Te_3, but the values calculated using density functional theory (DFT) are in good agreement with the values extrapolated from the temperature-dependent experimental work. The Bi_2Te_3 alloy has the same space group ($R\bar{3}m$) as the materials explored in the present work, which consist of six atoms along the [0001] direction, whereas the Bi_2Te_3 alloy has only five atoms along the same direction. The hexagonal structure of Bi_2Te_3 is known to be stable, but there are trigonal and rhombohedral phases of bismuth tellurides that are also stable with the concentrations of BiTe and Bi_4Te_3, respectively [18,21].

The growth and formation of $Bi_{1-x}Sn_x$ materials (which have two known phases: the rhombohedral structure of Bi and the body-centered tetragonal structure of β-Sn) have been investigated through experiment, along with their stability as potential solder joints [22,23]. There is a known tetragonal phase BiSn alloy that is discussed in the literature [24], but the energy is considerably above the convex hull. Temperature variations of the elastic properties of certain anisotropic Bi-Sn alloys were previously reported [25]. It was found that Bi-Sn solder alternatives will maintain strength and microstructure similar to Pb-based solder, reduce whisker formation due to stress, and reduce the weight of the product while maintaining similar cost [26,27]. Previous work also introduced the potential of ternary alloys using Bi and Sn in conjunction with Pb, Ag, or In to create a more stable alloy [23,28]. When alloying

*Corresponding author: msmeu@binghamton.edu

Bi-Sn with In, this ternary alloy maintains the same phase as the original binary alloy (rhombohedral or body-centered tetragonal) [28]. Previous analysis of the convex hull for Bi-In alloys showed stable tetragonal phases of BiIn and Bi_3In_5 and a hexagonal phase of $BiIn_2$ [24]. It has been shown in other systems that the inclusion of temperature can alter the phonon spectra of different materials [29], which can then affect the elastic properties of those materials. Temperature is an important factor in determining ductility [30]; however, for the materials studied in this work we are interested in an investigation of the effects of atomic substitution, as opposed to the effect of temperature.

In this work we use first-principles DFT calculations to study the elastic properties of different Bi-based alloys of the form $Bi_{1-x}Z_x$ (Z = Sb, Te, In, Sn; $0 \leqslant x \leqslant 1$). Through an investigation of the bulk (K), shear (G), and Young's (E) moduli, along with Poisson's ratio ν and the Pugh ratio ($\gamma = K/G$), we will discuss the effect of the alloy proportions on the properties of Bi. Through Bader charge analysis and comparative charge density analysis of each alloy, we show how changes in bonding impact the properties of these materials. Finally, because of the relatively large size of Bi, which results in strong spin-orbit coupling (SOC) [31,32], we investigate the effects of SOC on the elastic properties of the alloys.

II. COMPUTATIONAL METHODS

A. Elastic properties

The Pugh ratio is the calculated quantity related to ductility that is considered in this work. The Pugh ratio is a dimensionless quantity defined as the ratio of the bulk modulus to the shear modulus of a material; it has been found that this ratio yields information about the ductility of that material because it assigns a numerical value for ductility, which can then be used for comparison to known materials [33]. A material with a Pugh ratio greater than 1.75 is considered to be ductile, while a material that has a Pugh ratio less than 1.75 is considered to be brittle [33]. Although Pugh's original works were related to phenomenological findings, the Pugh ratio is readily used as a computational tool for predicting ductility. While not an all-encompassing quantity (as it is a ratio of other properties, not a uniquely calculated descriptor), it is very useful as it allows one to quantitatively assign ductility based on a single value calculated from first principles.

B. Computational details

The hexagonal crystal structure for Bi can be seen in Fig. 1(a). This unit cell has six unique sites that are available for substitution during the alloy process; each site was tested to confirm that the properties were calculated for the lowest-energy state in the hexagonal crystal structure. For all concentrations, each possible configuration of the ordered hexagonal structure was fully relaxed, after which the most energetically favorable configuration was chosen for the calculations that followed. The results of this site testing can be seen in Figs. 1(b)–1(f), and all relevant structural data for each alloy are shown in Supplemental Material Tables S7– S26 [34].

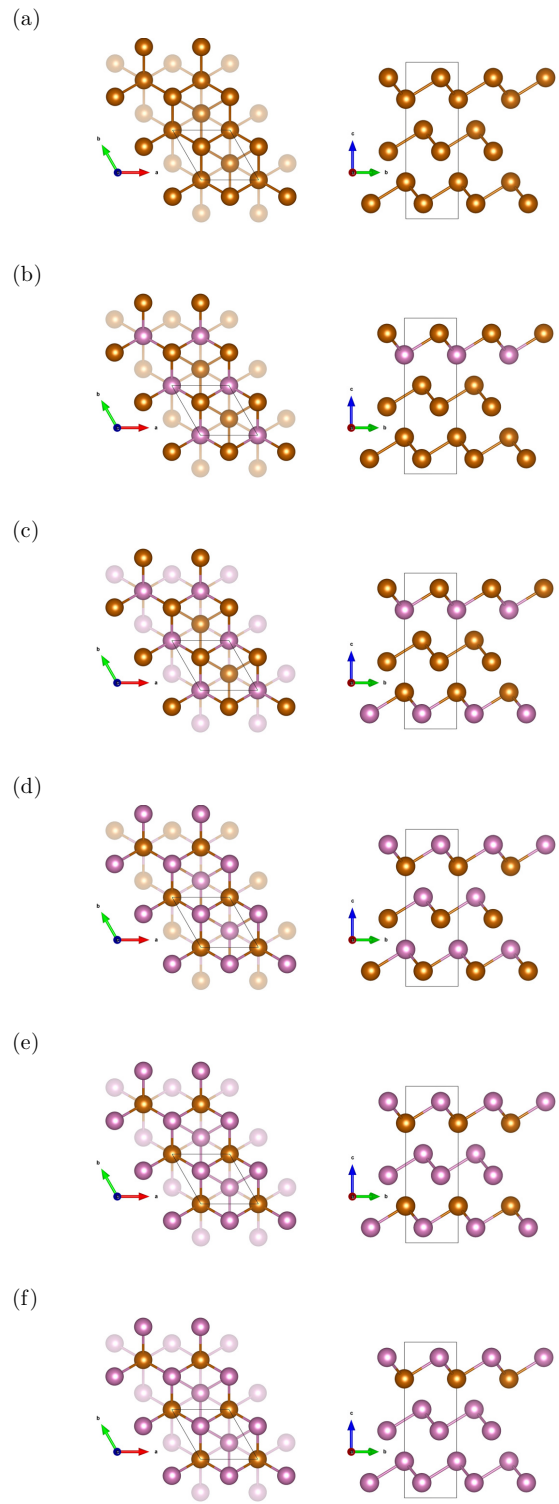

FIG. 1. Top (left column) and side (right column) views of $Bi_{1-x}Z_x$ crystal structure where (a) $x = 0$, (b) $x = 0.17$, (c) $x = 0.33$, (d) $x = 0.5$, (e) $x = 0.67$, and (f) $x = 0.83$. Orange atoms are Bi; pink atoms represent Z. Directions are as follows: $a = [2\bar{1}\bar{1}0]$, $b = [\bar{1}2\bar{1}0]$, and $c = [0001]$.

Each of the investigated materials was fully relaxed, and the elastic tensor was computed using DFT [35,36] as implemented in the Vienna Ab initio Simulation Package (VASP) [37–39]. VASP uses a plane-wave basis set, and ion-electron

interactions were approximated using the projector augmented wave potentials [40]. Both the kinetic energy cutoff and k-point grid were tested, with the criterion for convergence being an energy variation of less than 1 meV/atom. The reciprocal space was sampled using a Γ-centered Monkhorst-Pack k-point grid [41]. It was found that $15 \times 15 \times 5$ is a sufficient k-point grid for sampling the reciprocal space of the Bi crystal structure. The Brillouin zone was sampled by the Methfessel and Paxton method [42], and all structural relaxations and energy calculations were performed using the Perdew-Burke-Ernzerhof functional [43]. A plane-wave energy cutoff of 450 eV was found to be sufficient for this work.

Upon completion of the structural and electronic relaxations, the formation energy E_{Form} of each alloy was calculated:

$$E_{\text{Form}} = \frac{E_{\text{alloy}} - mE_{\text{Bi}} - nE_Z}{m+n}, \tag{1}$$

where E_{alloy} is the energy of the relaxed alloy, E_{Bi} is the energy per atom of Bi in its ground state, E_Z is the energy per alloy atom in its ground state, and m and n are the numbers of Bi atoms and alloy atoms in the $Bi_{1-x}Z_x$ structure, respectively. These calculations provide insight into the stability of the alloys investigated in this work. When $E_{\text{Form}} \leqslant 0$, these structures are potentially stable.

The elements of the elastic tensor C_{ij} are determined through the generalized stress-strain variant of Hooke's law:

$$\sigma_i = C_{ij}\epsilon_j, \tag{2}$$

where σ_i and ϵ_j are the tensile stress and longitudinal strain, respectively. After the elastic tensor is calculated, the bulk modulus K and the shear modulus G can be found using the following equations, respectively:

$$K_V = \frac{1}{9}(C_{11}+C_{22}+C_{33}) + \frac{2}{9}(C_{12}+C_{23}+C_{13}), \tag{3}$$

$$G_V = \frac{1}{15}(C_{11}+C_{22}+C_{33}) - \frac{1}{15}(C_{12}+C_{23}+C_{13}) + \frac{1}{5}(C_{44}+C_{55}+C_{66}). \tag{4}$$

By the nature of this calculation, these will provide the upper bounds for the quantities that are being computed. In order to obtain the lower bound, a slight variation of the equations must be used:

$$\frac{1}{K_R} = (S_{11}+S_{22}+S_{33}) + 2(S_{12}+S_{23}+S_{13}), \tag{5}$$

$$\frac{1}{G_R} = \frac{4}{15}(S_{11}+S_{22}+S_{33}) - \frac{4}{15}(S_{12}+S_{23}+S_{13}) + \frac{1}{5}(S_{44}+S_{55}+S_{66}), \tag{6}$$

where S_{ij} corresponds to the matrix elements of the inverse of the elastic tensor (i.e., the compliance tensor). When the lower bound is obtained, it will be multiplied with the upper bound, and a square root will be taken in order to give us a single value to report for each property. This method of processing the elastic tensor is known as the Voigt-Reuss-Hill approximation [44], which allows for the approximation of polycrystalline properties from single-crystal data. After the bulk and shear moduli are calculated, other physical properties can be computed, including Young's modulus E, Poisson's ratio ν, and the Pugh ratio γ:

$$E = \frac{9KG}{3K+G}, \tag{7}$$

$$\nu = \frac{3K-2G}{2(3K+G)}, \tag{8}$$

$$\gamma = \frac{K}{G}, \tag{9}$$

where γ is used to estimate the ductility of different materials.

Bader charge density analysis was also carried out based on the calculated charge densities from VASP using the code from the Henkleman group [45–48]. All structures were modeled using the Visualization for Electronic and Structural Analysis (VESTA) [49]. VESTA was also used to visualize the charge densities and the effective charge differences of each alloy.

TABLE I. Formation energy per atom of each investigated alloy, where Z = Sb, Te, In, Sn.

	E_{Form} (meV/atom)			
Material	Sb	Te	In	Sn
$Bi_{0.83}Z_{0.17}$	9	−1	194	40
$Bi_{0.67}Z_{0.33}$	11	−68	331	57
$Bi_{0.50}Z_{0.50}$	14	−132	453	64
$Bi_{0.33}Z_{0.67}$	11	−90	636	67
$Bi_{0.17}Z_{0.83}$	9	−40	786	70

III. RESULTS AND DISCUSSION

A. Crystal structure and stability

The purpose of this work is to determine the effect of alloying on the elastic properties of the hexagonal Bi crystal structure; for this reason atomically ordered structures have been used for all calculations in this work. It should be noted that the degree of order/disorder in a system can alter the outcome of the calculated elastic properties and formation energies, although it was not considered in this work [50]. Of the materials chosen to alloy with Bi (Sb, Te, In, Sn), only Sb shares the same bulk crystal structure with Bi. The bulk crystal structures for the other proposed materials are trigonal (Te), body-centered tetragonal (In), and diamond cubic (Sn). Because of the two possible configurations (when $x = 1$, the material could be in the hexagonal crystal structure of Bi, or it could be in the native structure of the dopant material), calculations of all elastic properties of the Bi_0Z_1 materials were performed in both crystal structures for the sake of comparison, and each of those values are also reported. The results of the E_{Form} calculations are shown in Table I. It is noted that the $Bi_{1-x}In_x$ and $Bi_{1-x}Sn_x$ alloys would be unlikely to form, but $Bi_{1-x}Sb_x$ and $Bi_{1-x}Te_x$ would form metastable (or possibly stable) materials.

We also considered the possibility of dopant atoms to occupy interstitial sites within the Bi crystal structure. For this work, six locations were chosen throughout the unit cell, and the dopant atoms were placed there. The material was allowed

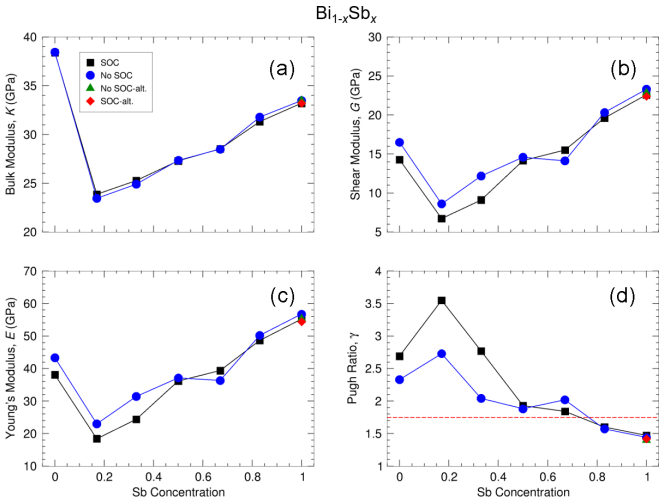

FIG. 2. (a) Bulk modulus, (b) shear modulus, (c) Young's modulus, and (d) Pugh ratio of $Bi_{1-x}Sb_x$ alloys with (squares) and without (circles) SOC. The alternate data points are for Sb in the hexagonal crystal structure with (diamonds) and without (triangles) SOC. Here the dotted line represents the boundary value (1.75) between brittle and ductile.

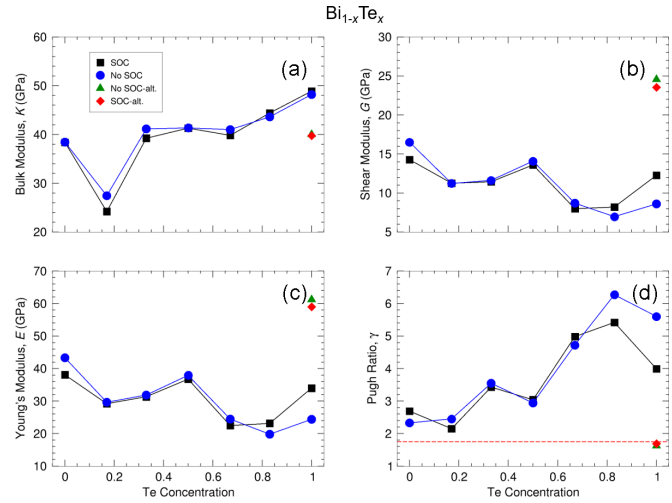

FIG. 3. (a) Bulk modulus, (b) shear modulus, (c) Young's modulus, and (d) Pugh ratio of $Bi_{1-x}Te_x$ alloys with (squares) and without (circles) SOC. The alternate data points are for Te in the trigonal crystal structure with (diamonds) and without (triangles) SOC. Here the dotted line represents the boundary value (1.75) between brittle and ductile.

to fully relax, and the formation energy of these materials was compared to those of the alloy material; it was determined that it was not favorable for the dopants to occupy interstitial sites.

B. Elastic properties

As a validation of the computational technique, calculations were carried out on several known materials to evaluate agreement with experiment. The materials tested were gold, diamond (C), copper, silver, nickel, and platinum. Because these materials have known property values, the computational technique could be verified, and the effect of SOC could also be tested. The results of this validation process are shown in Supplemental Material Table S1 [34]. Included in these results are the calculated elastic properties for each of the Z materials needed for the $Bi_{1-x}Z_x$ alloys. For all materials, we find that there is strong agreement with and without the use of SOC in the calculation of the elastic properties.

For all bulk materials used to verify the computational technique (reported in Supplemental Material Table S1 [34]), the Pugh ratio correctly predicts whether that material is ductile or brittle, apart from Bi and Te. However, the calculated bulk, shear, and Young's moduli for Bi are in agreement with experimental results. It was previously found that the properties of Te are highly dependent on temperature and pressure, which could explain the discrepancy in the calculated results [51]. We next calculated the elastic properties of $Bi_{1-x}Sb_x$ alloys. We find that the bulk and shear moduli [Figs. 2(a) and 2(b), respectively] undergo a very large drop upon the initial alloying of Bi with Sb. Because the change in G is more substantial than the change in K, there is an effective increase in the ductility, as determined by the Pugh ratio [Fig. 2(d)]. After this drastic change we find that as the amount of Sb in the system increases, the brittleness of the system also increases due to the brittle nature of Sb. Because Sb and Bi share the same crystal structure, valence electron configuration, and electronegativity values, it is reasonable that the system (which provides an incorrect γ value for bulk Bi) would have a relatively gradual change in its elastic properties as the concentration of Sb increases. By definition, a high Young's modulus [Fig. 2(c)] also corresponds to a stiff material. Thus, the inverse relationship between E and γ confirms the increase in brittleness at higher concentrations of Sb. This is in very close agreement with a previously performed computational investigation [7].

Next, we investigated the elastic properties of $Bi_{1-x}Te_x$ alloys. After an initial drop in K for the Te alloys [Fig. 3(a)], we find that K remains relatively constant as the concentration of Te increases; however, significant fluctuations in G [Fig. 3(b)] lead to noticeable changes in the ductility of the $Bi_{1-x}Te_x$ alloys. G inversely affects γ; thus, the overall decrease in G results in an increase in ductility [Fig. 3(d)] as the concentration of Te increases. Compared to Sb, the inverse relationship between E and γ is not as obvious. Instead, comparing Figs. 3(c) and 3(d), we find that below concentrations of $x = 0.5$, the quantities follow similar trends, but when $x \geqslant 0.5$, the inverse relationship is intact. There are significant differences in all the elastic properties for the two possible configurations shown at $x = 1$, which imply that Te is not inherently brittle, but the ductility is greatly dependent on the structure.

Because it has been so extensively studied and has a structure similar to the Bi-based alloys discussed in this work, the elastic properties of a layered phase of Bi_2Te_3 were also calculated. This structure has a hexagonal pattern similar to the example shown in Fig. 1(d); however, a layer of Bi has been removed. The results for this structure can be seen in Supplemental Material Table S1 [34]. We have found that for this particular concentration G and E provide results similar to those of the $Bi_{0.33}Te_{0.67}$ alloy which was studied, but the value of K is significantly different. This leads to a

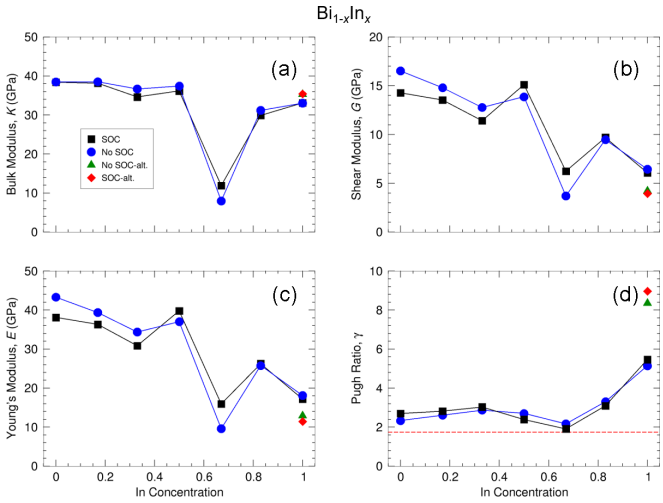

FIG. 4. (a) Bulk modulus, (b) shear modulus, (c) Young's modulus, and (d) Pugh ratio of $Bi_{1-x}In_x$ alloys with (squares) and without (circles) SOC. The alternate data points are for In in the body-centered tetragonal crystal structure with (diamonds) and without (triangles) SOC. Here the dotted line represents the boundary value (1.75) between brittle and ductile.

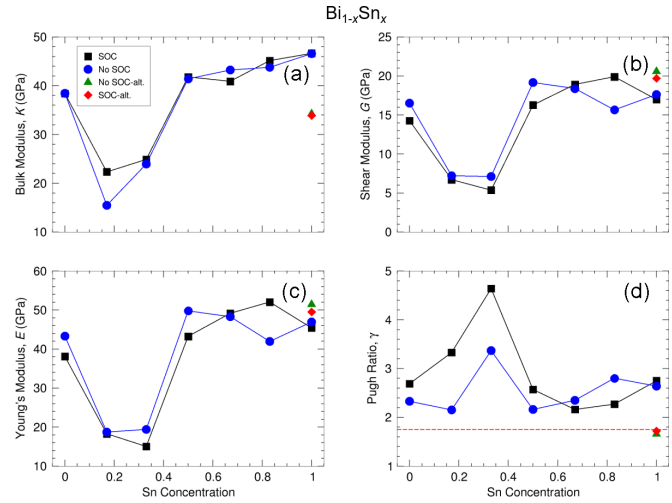

FIG. 5. (a) Bulk modulus, (b) shear modulus, (c) Young's modulus, and (d) Pugh ratio of $Bi_{1-x}Sn_x$ alloys with (squares) and without (circles) SOC. The alternate data points are for Sn in the diamond cubic crystal structure with (diamonds) and without (triangles) SOC. Here the dotted line represents the boundary value (1.75) between brittle and ductile.

drastically reduced value of γ (1.45 and 1.25, with and without SOC, respectively), indicating that at 0 K, this material is predicted to be brittle. While in good agreement with other computational values, the elastic moduli differ significantly relative to the experimental values for Bi_2Te_3 [52,53], further increasing the notion that the temperature dependence of these properties can play a significant role.

We then investigated the elastic properties of $Bi_{1-x}In_x$ alloys. As seen in Fig. 4, the properties have only slight variations when $x < 0.67$. At higher concentrations of In, the properties fluctuate significantly, indicating that certain concentrations of In could provide an increase in ductility, but the overall nature of the change is seemingly less predictable than in the other materials. The calculations of the Bi_0In_1 properties are of interest because in Figs. 4(a)–4(c), the properties of In in the hexagonal crystal structure are consistent with the properties of In in the body-centered tetragonal structure. However, the Pugh ratio [Fig. 4(d)] is drastically reduced when it is in the hexagonal crystal structure. Similar to Sb, E and γ for the $Bi_{1-x}In_x$ alloys [Figs. 4(c) and 4(d), respectively] obey an inverse relationship, confirming the drastic increase in ductility at higher concentrations of In. For the alloy materials being discussed in this work, In (1.7) has the largest difference in electronegativity from Bi (1.9); In also has two fewer valence electrons than Bi. It is not until a sufficient concentration of In is reached that the Bi bonds will weaken, leading to an increase in ductility (*vide infra*).

Finally, we investigated the elastic properties of $Bi_{1-x}Sn_x$ alloys. Low concentrations of Sn greatly alter the properties of the Bi-based system [as seen in Figs. 5(a)–5(c)]. This overall impact leads to a substantial increase in the Pugh ratio for $Bi_{0.67}Sn_{0.33}$ even though K, G, and E are drastically reduced at that concentration compared to Bi and Sn in their bulk forms. Apart from that spike, Fig. 5(d) shows that the ductility of $Bi_{1-x}Sn_x$ alloys is relatively constant. As with Te, there is a change from brittle to ductile which occurs for Bi_0Sn_1, showing the significance of crystal structure on the nature of that material. The changes in K are consistent with previous experimental results [54].

For each of the compounds discussed in Fig. 2–5, there is a direct correlation between G and E, despite the dependence of E on K. We find that G determines the trend of Young's modulus, but K determines the magnitude.

The effect of SOC on the elastic properties of the materials is most notably visible when looking at the Pugh ratio because of the compounding effect of the differences between K and G. These effects are most significant at high concentrations of Bi with Sb and Sn, which can be seen in Figs. 2(d) and 5(d), respectively. In each of these cases, the general trend of the Pugh ratio is maintained, but the magnitude of the value is significantly decreased without the inclusion of SOC. The numerical results of all property calculations are shown in Supplemental Material Table S2 [34].

C. Charge analysis

Bader charge analysis was performed on each of the alloys in this work to determine the significance of electron redistribution on the elastic properties of the materials. The Bader charges give a quantitative measure of how the charge on each atom has changed as the concentration of Bi decreases. The results are shown in Supplemental Material Tables S3–S6 [34]. Investigating the charge on the Bi atoms upon the initial substitute atom being added ($Bi_{0.83}Z_{0.17}$), for each of the possible alloy materials, we show that some Bi atoms gain charge, while other atoms lose charge, reducing the uniformity of charge distribution. However, as the concentration of Bi decreases (when $x \geqslant 0.50$) for each material, the changes in charge on the Bi atoms are uniformly distributed. In contrast to the quantitative approach, a visual investigation of the comparative charge density of each of our alloys compared

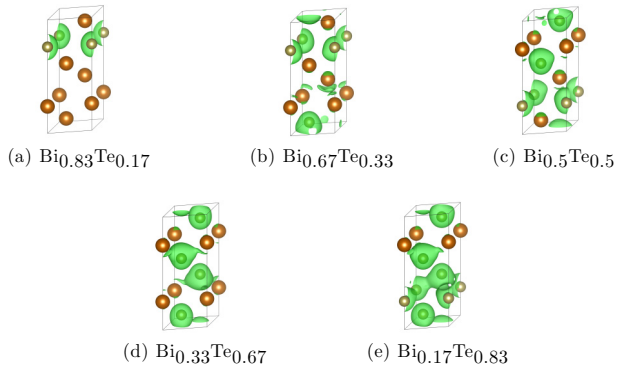

(a) $Bi_{0.83}Te_{0.17}$ (b) $Bi_{0.67}Te_{0.33}$ (c) $Bi_{0.5}Te_{0.5}$

(d) $Bi_{0.33}Te_{0.67}$ (e) $Bi_{0.17}Te_{0.83}$

FIG. 6. Comparative charge density plots of the $Bi_{1-x}Te_x$ alloys, with isosurface value $0.01e$. Orange atoms are Bi; gold atoms are Te. Green signifies an increase in electron density compared to bulk Bi.

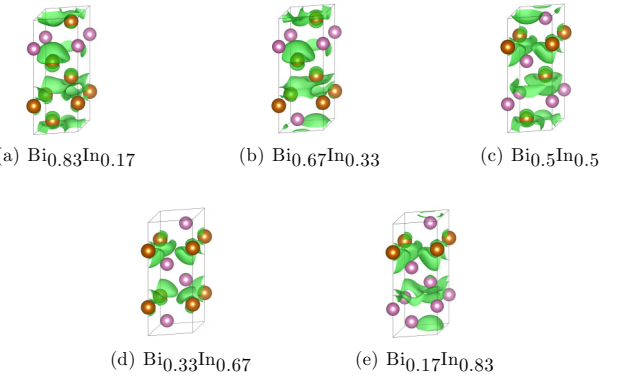

(a) $Bi_{0.83}In_{0.17}$ (b) $Bi_{0.67}In_{0.33}$ (c) $Bi_{0.5}In_{0.5}$

(d) $Bi_{0.33}In_{0.67}$ (e) $Bi_{0.17}In_{0.83}$

FIG. 8. Comparative charge density plots of the $Bi_{1-x}In_x$ alloys, with isosurface value $0.003e$. Orange atoms are Bi; pink atoms are In. Green signifies an increase in electron density compared to bulk Bi.

to the charge density of bulk Bi was performed such that a qualitative assessment of the effects could be made. With this we have also gained insight into the effect that changes in electron density will have on the ductility of a material. In general, a more uniform and delocalized charge density is indicative of improved ductility, while more localized charge density is not [55–57].

Shown in Figs. 6–9 are comparative charge density plots for each of the alloys investigated in this work. Figure 6 shows how the charge density distribution changes as Te is added to the Bi crystal structure; this can be compared to the Pugh ratio shown in Fig. 3(d). The comparative charge density in Fig. 6(a) is used as a reference point for the remainder of Fig. 6. Moving from Fig. 6(a) to Fig. 6(b), there is an increase in the number of locations showing a greater amount of charge density, which coincides with a small increase in the ductility. Increasing the concentration [Fig. 6(c)] does not show a significant change in charge density or Pugh ratio. At higher concentrations of Te [Figs. 6(d)–6(e)], the charge density increases notably and becomes increasingly delocalized. These changes correlate with an increase in ductility.

The changes in ductility for the $Bi_{1-x}Sn_x$ alloys [Fig. 5(d)] can also be explained using the comparative charge density plots shown in Fig. 7. Again, we use Fig. 7(a) as a reference point of charge density difference and ductility. From this point there is a drastic change in ductility associated with the large, diffuse charge density shown in Fig. 7(b). This transitions to a localized amount of charge difference that has drastically decreased in magnitude in Fig. 7(c). A decrease in ductility is confirmed in the Pugh ratio of $Bi_{0.5}Sn_{0.5}$. As the concentration of Sn is increased, the Pugh ratio remains relatively constant, and the comparative charge densities are also constant [Figs. 7(d)–7(e)].

As shown in Fig. 4(d), for low concentrations of In ($x \leqslant 0.5$), there are no significant changes to the Pugh ratio. The constant value of γ is consistent with the comparative charge density plots shown for the corresponding alloys [Figs. 8(a)–8(c)]. For $Bi_{0.33}In_{0.67}$ there is a noticeable decrease in ductility. At this concentration, the distribution of the charge density difference is smaller and more localized than for the high Bi concentrations [Fig. 8(d)]. But as the amount of In is increased, the comparative charge density diffuses and increases in magnitude [Fig. 8(e)], and the Pugh ratio increases.

Upon initial inspection, Figs. 9 and 2(d) provide a contradictory argument to the previously discussed materials. When

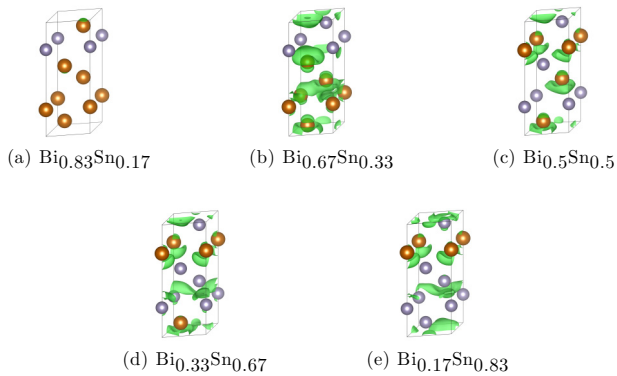

(a) $Bi_{0.83}Sn_{0.17}$ (b) $Bi_{0.67}Sn_{0.33}$ (c) $Bi_{0.5}Sn_{0.5}$

(d) $Bi_{0.33}Sn_{0.67}$ (e) $Bi_{0.17}Sn_{0.83}$

FIG. 7. Comparative charge density plots of the $Bi_{1-x}Sn_x$ alloys, with isosurface value $0.008e$. Orange atoms are Bi; gray atoms are Sn. Green signifies an increase in electron density compared to bulk Bi.

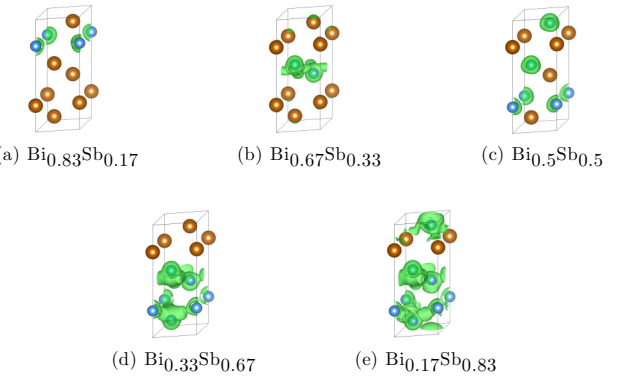

(a) $Bi_{0.83}Sb_{0.17}$ (b) $Bi_{0.67}Sb_{0.33}$ (c) $Bi_{0.5}Sb_{0.5}$

(d) $Bi_{0.33}Sb_{0.67}$ (e) $Bi_{0.17}Sb_{0.83}$

FIG. 9. Comparative charge density plots of the $Bi_{1-x}Sb_x$ alloys, with isosurface value $0.0045e$. Orange atoms are Bi; blue atoms are Sb. Green signifies an increase in electron density compared to bulk Bi.

looking at the Pugh ratio, starting with $Bi_{0.83}Sb_{0.17}$, there is a steady decrease in the predicted ductility of the alloys as the concentration of Sb increases. Yet the adjoining comparative charge densities show an increase in charge density difference as the amount of Sb increases. In contrast to the previous materials discussed, even though these charge densities are increasing, they are staying localized among the Sb atoms and are not interacting with the Bi atoms. For the higher concentrations [Figs. 9(d) and 9(e)] this is less obvious because the majority of the cell is Sb, but in the lower concentrations it is clear. Using Fig. 9(a) as the initial reference, there is no change in charge density between the Bi and Sb. Increasing the amount of Sb, we show a significant amount of charge density increase between the two Sb atoms in Fig. 9(b) when the Sb atoms are immediately adjacent to one another. Further increasing the concentration of Sb [Fig. 9(c)], the comparative charge density becomes drastically more localized. This leads to an inherent increase in brittleness as the amount of Sb is increased.

IV. SUMMARY AND CONCLUSIONS

In this work we investigated 20 unique Bi-based alloys of varying concentrations. We have found through the calculation of formation energies that each of the $Bi_{1-x}Te_x$ materials investigated is energetically favorable, and all of the $Bi_{1-x}Sb_x$ alloys are potentially metastable. The elastic properties were computed for each of the alloys, as well as for their bulk components. When calculating the elastic properties of the alloys, the effects of SOC were also considered, and it was determined that the use of SOC is necessary for each of these materials, regardless of concentration. For each element being alloyed with Bi, the properties were calculated in the hexagonal crystal structure, as well as the known crystal structure for that element. While not energetically favorable, it was found that holding Te and Sn in the hexagonal crystal structure would drastically alter their elastic properties and lead to a significant increase in ductility. We have detailed the effect that the charge density distribution has on the properties of the alloys by comparing the changes and how they relate to the Pugh ratio γ. By this analysis, it has been determined that an increase in diffusivity and delocalization of the charge density will lead to an increase in ductility. In summary, we have shown that there are many possible materials and concentrations which would allow us to increase the ductility of Bi, with low concentrations of Sn and Te providing the most beneficial changes in ductility while maintaining a high concentration of Bi.

ACKNOWLEDGMENTS

This work was supported by the Integrated Electronics Engineering Center (IEEC) at Binghamton University. This work was performed using the Spiedie HPC cluster at Binghamton University and the Texas Advanced Computing Center (TACC), a part of the Extreme Science and Engineering Discovery Environment (XSEDE), which is supported by NSF Grant No. ACI-1548562 under allocation TG-DMR180009. We thank Dr. J. Cho in the Department of Mechanical Engineering at Binghamton University for insightful discussions regarding this work.

[1] W. Haynes, *CRC Handbook of Chemistry and Physics*, 93rd ed. (Taylor and Francis, Boca Raton, USA, 2012).
[2] H. Black, Environ. Health Perspect. **113**, A682 (2005).
[3] O. A. Ogunseitan, JOM **59**, 12 (2007).
[4] P. Kapitza, Proc. R. Soc. London, Ser. A **119**, 358 (1928).
[5] M. F. Stroud and H. Wilman, Br. J. Appl. Phys. **14**, 381 (1963).
[6] G. Motoyasu, H. Kadowaki, H. Soda, and A. McLean, J. Mater. Sci. **34**, 3893 (1999).
[7] S. Singh, I. Valencia-Jaime, O. Pavlic, and A. H. Romero, Phys. Rev. B **97**, 054108 (2018).
[8] Y. Kariya and M. Otsuka, J. Electron. Mater. **27**, 1229 (1998).
[9] J.-W. Choi, H.-S. Cha, and T.-S. Oh, Mater. Trans. **43**, 1864 (2005).
[10] J. Cho, S. Mallampati, R. Tobias, H. Schoeller, L. Yin, and D. Shaddock, in *2016 IEEE 66th Electronic Components and Technology Conference (ECTC)* (Institute of Electrical and Electronics Engineers, Piscataway, 2016), pp. 432–437.
[11] A. Datta and G. S. Nolas, Cryst. Eng. Commun. **13**, 2753 (2011).
[12] H. Zhang, J. S. Son, J. Jang, J. S. Lee, W. L. Ong, J. A. Malen, and D. V. Talapin, ACS Nano **7**, 10296 (2013).
[13] K. Kaspar, K. Fritsch, K. Habicht, B. Willenberg, and H. Hillebrecht, J. Electron. Mater. **46**, 92 (2017).
[14] J. P. Dismukes, R. J. Paff, R. T. Smith, and R. Ulmer, J. Chem. Eng. Data **13**, 317 (1968).
[15] H. Y. Lv, H. J. Liu, L. Pan, Y. W. Wen, X. J. Tan, J. Shi, and X. F. Tang, J. Phys. Chem. C **114**, 21234 (2010).
[16] S. Lee, K. Esfarjani, J. Mendoza, M. S. Dresselhaus, and G. Chen, Phys. Rev. B **89**, 085206 (2014).
[17] S. Singh, W. Ibarra-Hernández, I. Valencia-Jaime, G. Avendaño-Franco, and A. H. Romero, Phys. Chem. Chem. Phys. **18**, 29771 (2016).
[18] J. Jenkins, J. Rayne, and R. Ure, Phys. Rev. B **6**, 1609 (1972).
[19] B.-L. Huang and M. Kaviany, Phys. Rev. B **77**, 125209 (2008).
[20] Y. Tong, F. Yi, L. Liu, P. Zhai, and Q. Zhang, Comput. Mater. Sci. **48**, 343 (2010).
[21] P. W. Lange, Naturwissenschaften **27**, 133 (1939).
[22] A. K. Gain and L. Zhang, J. Mater. Sci. Mater. Electron. **27**, 781 (2016).
[23] M. Kamal, B. M. Moharram, H. Farag, A. El-Bediwi, and H. F. Abosheiasha, Radiat. Eff. Defects Solids **161**, 421 (2006).
[24] T. Massalski and H. Okamoto, *Binary Alloy Phase Diagrams*, 2nd ed. (ASM International, Ohio, 1990).
[25] H. Kamioka, Jpn. J. Appl. Phys. **22**, 1805 (1983).
[26] W. R. Osório, L. C. Peixoto, L. R. Garcia, N. Mangelinck-Noël, and A. Garcia, J. Alloys Comp. **572**, 97 (2013).

[27] N. Jadhav, M. Williams, F. Pei, G. Stafford, and E. Chason, J. Electron. Mater. **42**, 312 (2013).
[28] R. M. Shalaby, Mater. Sci. Eng. A **560**, 86 (2013).
[29] A. H. Romero, E. K. U. Gross, M. J. Verstraete, and O. Hellman, Phys. Rev. B **91**, 214310 (2015).
[30] G. Leibfried and W. Ludwig, in *Theory of Anharmonic Effects in Crystals*, edited by F. Seitz and D. Turnbull, Solid State Physics Vol. 12 (Academic, 1961), pp. 275–444.
[31] F. Herman, C. D. Kuglin, K. F. Cuff, and R. L. Kortum, Phys. Rev. Lett. **11**, 541 (1963).
[32] T. Hirahara, T. Nagao, I. Matsuda, G. Bihlmayer, E. V. Chulkov, Y. M. Koroteev, P. M. Echenique, M. Saito, and S. Hasegawa, Phys. Rev. Lett. **97**, 146803 (2006).
[33] S. Pugh, London, Edinburgh Dublin Philos. Mag. J. Sci. **45**, 823 (1954).
[34] See Supplemental Material at http://link.aps.org/supplemental/10.1103/PhysRevB.100.104105 for Tables S1– S26 which provide information regarding materials used for verification of technique, Bader charge analysis data, and structural information relating to all alloys studied in this work .
[35] P. Hohenberg and W. Kohn, Phys. Rev. **136**, B864 (1964).
[36] W. Kohn and L. J. Sham, Phys. Rev. **140**, A1133 (1965).
[37] G. Kresse and J. Hafner, Phys. Rev. B **47**, 558 (1993).
[38] J. Furthmüller and G. Kresse, Comput. Mater. Sci. **6**, 15 (1996).
[39] G. Kresse and J. Furthmüller, Phys. Rev. B **54**, 11169 (1996).
[40] P. E. Blöchl, Phys. Rev. B **50**, 17953 (1994).
[41] J. D. Pack and H. J. Monkhorst, Phys. Rev. B **16**, 1748 (1977).
[42] M. Methfessel and A. T. Paxton, Phys. Rev. B **40**, 3616 (1989).
[43] J. P. Perdew, K. Burke, and M. Ernzerhof, Phys. Rev. Lett. **77**, 3865 (1996).
[44] R. Hill, Proc. Phys. Soc. London, Sect. A **65**, 349 (1952).
[45] G. Henkelman, A. Arnaldsson, and H. Jónsson, Comput. Mater. Sci. **36**, 354 (2006).
[46] W. Tang, E. Sanville, and G. Henkelman, J. Phys.: Condens. Matter **21**, 084204 (2009).
[47] M. Yu and D. R. Trinkle, J. Chem. Phys. **134**, 064111 (2011).
[48] E. Sanville, S. Kenny, R. Smith, and G. Henkelman, J. Comput. Chem. **28**, 899 (2007).
[49] K. Momma and F. Izumi, J. Appl. Crystallogr. **44**, 1272 (2011).
[50] D. Edström, D. G. Sangiovanni, L. Hultman, and V. Chirita, Thin Solid Films **571**, 145 (2014).
[51] A. De Vos and D. Van Dhelsen, Rev. Phys. Appl. **14**, 815 (1979).
[52] V. M. Prokhorov and G. I. Pivovarov, Ultrasonics **51**, 715 (2011).
[53] H. Koc, A. M. Mamedov, and E. Ozbay, in *2013 Joint IEEE International Symposium on Applications of Ferroelectric and Workshop on Piezoresponse Force Microscopy (ISAF/PFM)* (IEEE, 2016), pp. 41–44.
[54] L. Shen, P. Septiwerdani, and Z. Chen, Mater. Sci. Eng. A **558**, 253 (2012).
[55] T. Dasgupta, U. V. Waghmare, and A. M. Umarji, Phys. Rev. B **76**, 174110 (2007).
[56] M.-J. Lai, X.-Y. Xue, Z.-B. Zhou, B. Tang, J.-S. Li, and L. Zhou, J. Shanghai Jiaotong Univ. **16**, 227 (2011).
[57] H. Kindlund, D. G. Sangiovanni, L. Martinez-de Olcoz, J. Lu, J. Jensen, J. Birch, I. Petrov, J. E. Green, V. Chirita, and L. Hultman, APL Mater. **1**, 042104 (2013).